Published in final edited form as:
Phys Med Biol. 2009 May 21; 54(10): 3083–3099. doi:10.1088/0031-9155/54/10/008.

Evaluation of a compartmental model for estimating tumor hypoxia via FMISO dynamic PET imaging

Wenli Wang[1], **Jens-Christoph Georgi**[2], **Sadek A. Nehmeh**[1], **Manoj Narayanan**[3], **Timo Paulus**[2], **Matthieu Bal**[4], **Joseph O'Donoghue**[1], **Pat B. Zanzonico**[1], **C. Ross Schmidtlein**[1], **Nancy Y. Lee**[1], and **John L. Humm**[1]

Wenli Wang: wangw1@mskcc.org

[1]Memorial Sloan-Kettering Cancer Center, 1275 York Ave, New York, NY 10021, USA

[2]Philips Technologie GmbH Forschungslaboratorien, Molecular Imaging Systems, Weisshausstrasse 2, 52066 Aachen, Germany

[3]Philips Research North America, 345 Scarborough Rd, Briarcliff Manor, NY 10510, USA

[4]Philips Radiation Oncology Systems, 5520 Nobel Dr, Suite 125, Fitchburg, WI 53711, USA

Abstract

This paper systematically evaluates a pharmacokinetic compartmental model for identifying tumor hypoxia using dynamic positron-emission-tomography (PET) imaging with 18F-fluoromisonidazole (FMISO). A generic irreversible one-plasma two-tissue compartmental model was used. A dynamic PET image dataset was simulated with 3 tumor regions -- normoxic, hypoxic and necrotic, embedded in a normal-tissue background, and with an image-based arterial input function. Each voxelized tissue's time-activity-curve (TAC) was simulated with typical values of kinetic parameters, as deduced from FMISO-PET data from 9 head-and-neck cancer patients. The dynamic dataset was first produced without any statistical noise to ensure that correct kinetic parameters were reproducible. Next, to investigate the stability of kinetic parameter estimation in the presence of noise, 1000 noisy samples of the dynamic dataset were generated, from which 1000 noisy estimates of kinetic parameters were calculated and used to estimate the sample mean and covariance matrix. It is found that a more peaked input function gave less variation in various kinetic parameters, and the variation of kinetic parameters could also be reduced by two region-of-interest averaging techniques. To further investigate how bias in the arterial input function affected the kinetic parameter estimation, a shift error was introduced in the peak-amplitude and peak-location of the input TAC, and the bias of various kinetic parameters calculated. In summary, mathematical phantom studies have been used to determine the statistical accuracy and precision of model-based kinetic analysis, which helps to validate this analysis and provides guidance in planning clinical dynamic FMISO-PET studies.

Keywords

hypoxia; pharmacokinetics; compartmental modeling; positron emission tomography; ^{18}F-FMISO

1. Introduction

In normal tissues, there exists a homeostasis between oxygen supply from the capillary vasculature and oxygen consumption by tissue cells. In tumors, however, this homeostasis is frequently compromised, as uncontrolled cellular proliferation pushes cells further from blood vessels and into regions of progressively lower oxygen pressure (pO_2). As a consequence, the pO_2 within a tumor steadily decreases from physiologic levels at the capillary down to nearly

zero at the boundary region of tumor necrosis. This phenomenon is called chronic hypoxia. The other form of hypoxia is acute hypoxia. It occurs from a temporary decrease or arrest of normal flow in a tumor blood vessel, and thus results in temporary depletion of oxygen in the cells surrounding the blood vessel. Tumor hypoxia, especially chronic hypoxia, i.e., the near-zero oxygen concentrations adjacent to regions of tumor necrosis, has important clinical and radiobiological consequences.

Tumor hypoxia has been known to impair the effectiveness of radiotherapy for over 50 years (Thomlinson and Gray 1955). The recent surge of interest in non-invasive measurement of tumor hypoxia has arisen due to the increasing number of reports associating poor treatment response and poor prognosis with increased fractional volume of tumor hypoxia as assessed by pO_2 Eppendorf probe histography and other means. Höckel *et al* 1993 demonstrated significantly shorter overall and recurrence-free survival for patients with hypoxic cervical tumors (median $pO_2 < 10$ mmHg). Similar results have been reported in head-and-neck cancer by Nordsmark *et al* 1996 and Brizel *et al* 1997, in sarcoma by Brizel *et al* 1996, in cervical cancer by Fyles *et al* 1998 and Knocke *et al* 1999, and in prostate cancer by Movsas *et al* 1999. In addition to direct pO_2 probe measurement, there is extensive immunohistochemical evidence showing that higher expression of endogenous markers of hypoxia, e.g., VEGF and HIF-1 alpha, identify those prostate cancer patients at higher risk of biochemical failure (Vergis *et al* 2008). These findings underscore the potential utility in developing a more practical technique for the quantitative assessment of tumor hypoxia, for identifying predictors of tumor aggressive and stratifying patients who may respond more poorly to treatment (Tatum *et al* 2006).

Positron-emission-tomography (PET) measurement of tumor hypoxia offers the advantages of being non-invasive, repeatable and potentially providing a quantitative three-dimensional image of the hypoxic region. In addition, it eliminates erroneous results (i.e., false negatives) resulting from the limited tissue sampling associated with probe-based measurements and tissue section-based methods such as immunohistochemistry. A number of PET radiotracers with which to specifically image viable hypoxic cells in solid tumors have been developed. These include most notably the 2-nitroimidazole family of compounds: ^{18}F-labeled fluoro-misonidazole (^{18}F-FMISO) (Rasey *el al.* 1996, Rajendran *et al* 2003, Lee *et al* 2008), ^{18}F-fluoro-erythronitroimidazole (FETNIM) (Yang *et al* 1995, Lehtiö *et al* 2003 and 2004), 2-(2-nitro-1H-imidazol-1-yl)-N-(2,2,3,3,3-pentafluoropropyl)-acetamide (EF5) (Evans *et al* 2000, Ziemer *et al* 2003), ^{18}F-fluoroazomycin-arabinosise (^{18}F-FAZA) (Sorger *et al* 2003), and ^{124}I-labeled iodinated-azomycin-galactopyranoside (^{124}I-IAZGP) (Zanzonico *et al* 2004, Riedl *et al* 2008), as well as other tracers such as copper-diacetyl-bis(N^4)-methylthiosemicarbazone (Cu-ATSM) (Lewis *et al* 2001, Dehdashti *et al* 2003).

The most widely used hypoxia tracer in clinical studies is ^{18}F-FMISO. Its parent compound, misonidazole, a radiosensitizer similar to pimonidazole, is irreversibly bound in the cell under hypoxic conditions (Chapman *et al* 1989, Casciari *et al* 1995, Brown *et al* 1996). The drug is bioreductively activated by electron transport. The first-electron reaction produces the nitro radical anion, which is reversed in the presence of oxygen in the cell. In the absence of oxygen, however, a second electron reaction generates a bioreductive alkylation agent. This reduced FMISO bioreduction product then binds to macromolecules within the cell and is trapped over the time course of PET acquisition.

Clinical studies performed at the University of Washington have shown positive imaging of tumor hypoxia, but with low PET signal contrast. Analysis of the biodistribution of FMISO in patients imaged between 2 to 3 hours post-injection led to an operational definition of tumor hypoxia as corresponding to voxels having a tumor-to-blood activity concentration ratio of greater than 1.2–1.6 (Rasey *et al* 1996, Rajendran *et al* 2003, 2004 and 2006). One concern is

the slow and potentially variable clearance of FMISO from normal (i.e., normoxic) tissues relative to the 110-minute half-life of ^{18}F, which can lead to significant variability in PET images of hypoxia if segmented in the foregoing manner. Later PET imaging might lead to improved hypoxia-to-normoxia ratios, but incur the problem associated with poorer count statistics. An investigation of the variability in the hypoxia when applying segmentation to two baseline FMISO exams of the same set of 20 patients performed 3 days apart revealed considerable changes in the fraction of hypoxic voxels (Nehmeh *et al* 2008). The variability in tumor uptake of FMISO can be due to photon counting noise and/or acute tumor hypoxia.

In order to overcome the dependence on a single threshold criterion for discriminating hypoxic from non-hypoxic tumor sub-volumes, the current study investigates the feasibility of performing a pharmacokinetic compartmental analysis to model the transport and metabolism of the radiotracer uptake in tumors. The input required for such an analysis is dynamic PET imaging data for which region-of-interest (ROI) corresponding to tumor as well as arterial blood can be identified. The compartmental analysis tool used is based on a generic two-tissue model implemented in Philips Research's Voxulus software package, which is also included in the research version of Pinnacle^3™, Philips' radiation treatment planning software, and in IMALYTICS, Philips' preclinical research workspace. Voxulus is able to perform pharmacokinetic modeling for each image voxel as well as ROIs (i.e., contiguous groups of voxels). Prior investigations using this general approach have been published by Thorwarth *et al* 2005a and 2005b, who has already demonstrated the feasibility of compartmental analysis of dynamic FMISO data. The main purpose of this paper is to evaluate the feasibility of voxel-based compartmental analysis, tested using the one-plasma two-tissue irreversible compartmental model implemented within Voxulus.

2. Materials and Methods

2.1. Two-tissue compartmental model

The irreversible one-plasma two-tissue compartmental model (Huang and Phelps 1986) is shown in figure 1, where $C_p(t)$, $C_1(t)$ and $C_2(t)$ are activity concentration (unit in Bq/ml) as a function of time t (unit in min) post-administration in the plasma compartment, reversible tissue compartment and trapped tissue compartment, respectively; and k_1, k_2 and k_3 are kinetic reaction rate constants (unit in 1/min) between compartments.

The rate of activity concentration in these two tissue compartments is then modeled as

$$\begin{aligned}\frac{dC_1(t)}{dt} &= k_1 C_p(t) - (k_2+k_3)C_1(t)\\ \frac{dC_2(t)}{dt} &= k_3 C_1(t)\end{aligned} \tag{1}$$

By solving the above two differential equations, $C_1(t)$ and $C_2(t)$ can be expressed as

$$\begin{aligned}C_1(t) &= k_1 e^{-(k_2+k_3)t} \otimes C_p(t)\\ C_2(t) &= \frac{k_1 k_3}{k_2+k_3}\left[1 - e^{-(k_2+k_3)t}\right] \otimes C_p(t)\end{aligned} \tag{2}$$

where $\otimes$ denotes convolution. The activity concentration $C_{ROI}(t)$ in a given ROI is a weighted sum of $C_p(t)$, $C_1(t)$ and $C_2(t)$:

$$C_{ROI}(t) = \beta C_p(t) + C_1(t) + C_2(t) \tag{3}$$

where β is the fraction of vascular space (a scalar between 0 and 1) in the ROI compared with the plasma input function. The ROI can be a single image voxel or a group of image voxels.

In Voxulus, the plasma input function is modeled as an analytical function

$$C_p(t)=A_0te^{-C_0t} + \sum_{i=1}^{N} A_i \left(e^{-C_{1i}t} - e^{-C_{2i}t}\right), \quad (4)$$

where the unit of A_0 is Bq/(ml·min), of A_i Bq/ml, and of C_0, C_{1i}, C_{2i} 1/min. The input function parameters $\{A_0, C_0, A_i, C_{1i}, C_{2i}, i=1, \ldots, N\}$ can be estimated either from the arterial regions in the dynamic image dataset or from serial blood sampling.

Given the analytical ROI time-activity-curve (TAC) (3) with inserts (2) and (4), and a measured ROI TAC, a Levenberg-Marquardt least-square (LS) or weighted-least-square (WLS) optimization scheme is used in Voxulus to estimate the kinetic parameters $\{k_1, k_2, k_3, \beta\}$. The same optimization scheme is used for the input function parameters estimation. Note that for multiple-voxel ROI, Voxulus estimates each kinetic parameter on a voxel-by-voxel basis within the ROI, resulting in parametric images of each of the model parameters.

2.2. Physical interpretation of various tissue types

Inserting (2) into (3), the target tissue's TAC is modeled as the summation of three components, as shown in (5): (a) the direct contribution from the input function due to the vascular space within the tissue, $C_{ROI}^{Vascular}(t)$; (b) the reversible (i.e., diffusion) contribution of the input function, $C_{ROI}^{Diffused}(t)$, which is the convolution of an exponential function (with decay constant k_2+k_3) with the input function; (c) the irreversible or trapped contribution from the input function, $C_{ROI}^{Trapped}(t)$, which is the convolution of a constant step function with the input function.

$$\begin{aligned} C_{ROI}(t) &= C_{ROI}^{Vascular}(t)+C_{ROI}^{Diffused}(t)+C_{ROI}^{Trapped}(t) \\ \text{where } C_{ROI}^{Vascular}(t) &= \beta\, C_p(t) \\ C_{ROI}^{Diffused}(t) &= \frac{k_1k_2}{k_2+k_3}e^{-(k_2+k_3)t} \otimes C_p(t) \\ C_{ROI}^{Trapped}(t) &= \frac{k_1k_3}{k_2+k_3} \otimes C_p(t) \end{aligned} \quad (5)$$

Note that the irreversible two-tissue compartmental model is equivalent to a system of two decoupled single-tissue compartmental models, as shown in figure 2 (Blomquist 1990). The influx rate constant $\frac{k_1k_3}{k_2+k_3}$ from the plasma compartment to the trapped compartment is denoted as K_i. These $\{k_1, k_2, k_3, \beta, K_i\}$ are called kinetic parameters or kinetic rate constants.

For a bolus-injection plasma input function, both the vascular and diffused components decrease with time while the trapped component increases with time. For hypoxic tumor, the trapped component dominates the other two components; while for normoxic tumor, the trapped component is small compared with the remaining two; and for necrotic tumor, the trapped component is a compromise of the previous two cases (Thorwarth *et al* 2005a). Figure 3 displays a TAC of hypoxic tumor as a decomposition of three components.

2.3. Validation methods

To help select values of the kinetic parameters that reflect actual clinical situation, nine head-and-neck cancer patients' dynamic FMISO-PET data are analyzed with Voxulus and a representative set of kinetic parameters are estimated for the normoxic, hypoxic and necrotic tumor regions, and for the normal-tissue background region, respectively. A representative plasma input function is also derived from the dynamic image datasets from a region circumscribing the carotid artery. Figure 4(a) shows a patient's measured and fitted image-based input function. Figure 4(b) shows a patient's measured TACs of the tumor and background soft tissue regions, respectively. The actual time sampling points are shown as cross signs in these figures. The purpose of this paper is not to evaluate Voxulus using clinical data but to provide an analysis of the statistical reliability of voxel-based compartmental modeling using dynamic PET data.

Using equations (2)–(4), a dynamic image dataset is generated with 4 distinct regions corresponding to: plasma, normoxic tumor, hypoxic tumor and necrotic tumor embedded in a normal-tissue background. An illustration of the mathematical dynamic image phantom simulated in this work is shown in figure 5. Note that the plasma region corresponds to a fixed set of input parameters, and each tumor region and background region corresponds to a particular set of kinetic parameters.

2.3.1. Noise-free and noisy samples—The dynamic image dataset is first simulated without any statistical noise to serve as a consistency check of the Voxulus software, that is, to verify that the correct kinetic parameter values are indeed estimated. Next, to investigate the stability of this voxel-wise analysis in the presence of noise, 1000 noisy samples of the dynamic image data are generated. The noise at each voxel n and at each dynamic frame i is simulated as a Gaussian, with standard deviation $\sigma_{n,i}$ modeled as

$$\sigma_{n,i} = c\sqrt{f_{n,i} d_i / t_i^{dur}} \tag{6}$$

where $f_{n,i}$ is the activity concentration in the n^{th} image voxel and at the i^{th} dynamic frame after decay and frame-duration correction; $d_i = \exp(\lambda t_i)$ is the isotope decay correction factor, with λ the decay constant and t_i acquisition time at the i^{th} frame; t_i^{dur} is the duration time (in sec) at the i^{th} frame; thus $f_{n,i} t_i^{dur} / d_i$ represents the mean activity concentration before decay and duration correction; c is a constant which scales the Gaussian noise with standard deviation close to the clinical situation. In a reconstructed image with iterative reconstruction, the statistical noise obeys a multivariate log-normal distribution (Barrett *et al* 1994, Wilson *et al* 1994), which behaves more like a Gaussian than a Poisson distribution. In addition, there is slight correlation between nearby voxels. In this study, however, no such correlation is assumed.

2.3.2 %bias, %stddev and correlation coefficient—These 1000 samples of noisy data are first smoothed by a 3-point-boxcar-average filter in both the horizontal and vertical dimensions, run through Voxulus, and then 1000 noisy samples of the kinetic parameter images are estimated for each k_1, k_2, k_3 and β. For each tumor-tissue type, a central voxel is selected from the region and thus 1000 noisy samples for each kinetic parameter are obtained at that voxel. The percentage bias and percentage standard deviation are calculated with respect to the true value for each kinetic parameter and each tumor type, as shown below

$$\%bias = (\mu_{x_n} / x_n^{true} - 1) \times 100$$
$$\%stddev = (\sigma_{x_n} / x_n^{true}) \times 100 \quad (7)$$

where μ_{x_n}, σ_{x_n}, x_n^{true} are the sample mean, sample standard deviation and true value of a kinetic parameter x at the n^{th} voxel. The linear Pearson correlation coefficient $\rho(x_n, y_n)$ is computed for any two kinetic parameters x and y at the n^{th} voxel for each tumor type. The correlation coefficient is obtained by dividing the sample covariance of the two variables by the product of their sample standard deviations.

2.3.3. ROI-averaging—The kinetic parameters estimated from a single voxel inevitably have some statistical variation due to the noise in the dynamic data. To reduce noise, two ROI-average approaches are used. The first approach is called "estimate-and-average". That is, the kinetic parameters are first estimated for each voxel, then a ROI is selected for voxels having similar kinetic parameters, and the average kinetic parameters are obtained over the ROI. The second approach is called "average-and-estimate", where the TAC of the tumor region is first averaged over a pre-selected ROI, and then Voxulus is used to estimate the ROI TAC kinetic parameters. In clinical settings, the "estimate-and-average" approach would probably be preferred over the "average-and-estimate" approach, since averaging the ROI is easy to implement for the first approach when the kinetic parameters are already estimated. To investigate the stability of both ROI-average approaches, ROIs of different size are selected over the hypoxic tumor region, and the *%bias* and *%stddev* are then computed for each approach from these 1000 noisy samples. That is, the ROI *%bias* and *%stddev* are computed for each k_1, k_2, β, k_3 and K_i, as a function of ROI size for both approaches. Similarly, the *%bias* and *%stddev* are computed from the ROI TAC from the noisy dynamic dataset with respect to the true TAC. For the ROI TAC, the *%bias* and *%stddev* also depend on the dynamic frame. A late-time frame is used as the reference when reporting the statistics in the dynamic dataset and ROI TAC.

2.3.4. Impact of peak-to-tail ratio in input function—In clinical head-and-neck FMISO studies, the image-based input function method is used and the input region is selected from the carotid artery. The bolus injection speed affects the peak-to-tail ratio of the input function. The intensity threshold of voxels used in image-based input function also affects the peak-to-tail ratio of the input function. To investigate this effect, different peak-to-tail ratios of the input function are simulated, and the *%stddev* of various kinetic parameters is computed and compared with different sets of input function.

2.3.5. Impact of distortions in input function—To investigate how distortions in the input function affect the kinetic parameter estimation, a shift error is introduced in peak amplitude and peak location in time of the plasma input function, respectively, in the absence of noise. The *%bias* of various kinetic parameters is then computed.

3. Results

3.1. Mathematical phantom simulation

The simulated dynamic dataset consists of 14 frames with start acquisition time {0, 1, 2, 3, 4, 5, 10, 15, 20, 25, 90, 95, 180 and 185} minutes, respectively, where the first five frames have 1 minute duration time, and the rest frames have 5 minutes duration time. Figure 5 displays the dynamic images at multiple frames and their mid-frame acquisition time. The number of frames, acquisition time and duration time for each frame are selected from our FMISO head-and-neck cancer patient protocol. The plasma input function was simulated with *{A_0=3.66e*

+5 Bq/(ml·min), C_0=*3.42* 1/min, *N=2*, A_1=*2e+4* Bq/ml, C_{11}=*0.21* 1/min, C_{21}=*1.2* 1/min, A_2=*7e+3* Bq/ml, C_{12}=*2.4e-3* 1/min, C_{22}=*0.12* 1/min}, with its TAC shown in figure 6(a). The kinetic parameters for three tumor regions and background normal tissue region are shown in table 1, with their respective TACs shown in figure 6(b).

3.2. Noiseless and noisy cases

Without noise, the estimated input function parameters and kinetic parameters match the true values exactly.

After adding Gaussian noise (c=150 in (6)), at a level equivalent to that observed in typical clinical FMISO PET data acquired on GE Discovery STE scanner with axial septa, the *stddev* of the activity concentration in each voxel in the hypoxic tumor region at late dynamic frame is approximately *15%*. Table 2 shows the *%bias* and *%stddev* for a single voxel centered in each of three tumor regions and the background normal tissue region respectively with LS estimations. All kinetic parameters have less than *5 %bias*, except that β has 28.2 *%bias* in the necrotic tumor region where it has very small true value of *0.03*. In the hypoxic and necrotic tumor regions with high k_3 true value (*0.008* and *0.003*), the k_3 has comparable *%stddev* (*13.5* and *15.9*) with k_1 and k_2, but larger *%stddev* of *42.9* in normoxic tumor and *35.0* in normal tissue regions, where their true values are small (both are *0.001*). In regions of hypoxic and normoxic tumors with high β true value of *0.3*, its *%stddev* is *28*; in the background normal tissue region with medium β true value of *0.1*, its *%stddev* is *43.9*; while in the necrotic tumor region with small β true value *of 0.3*, its *%stddev* is *81.8*. Table 3 shows the correlation coefficient of various kinetic parameters for a single voxel centered in each of three tumor regions and the background normal tissue region respectively. We noticed that k_1 and k_2 are highly correlated; and both are negatively correlated with β; while k_3 has little correlation with k_1, k_2 or β.

We observed that the influx rate constant $K_i=\frac{k_1 k_3}{k_2+k_3}$ is potentially a more stable and direct hypoxia index than k_3. From the objective function of the pharmacokinetic model, it can be shown that K_i estimate is a linear function of the ROI's activity concentration, but not k_3. Thus, K_i is less sensitive to noise than k_3, e.g., the *%stddev* of K_i in hypoxia tumor region is *6.3* and of k_3 is *13.5*. K_i also has less correlation with β than k_3, e.g., the correlation coefficient of K_i in hypoxia tumor region is *−0.27* and of k_3 is *0.69*. Note that the physical interpretation of K_i denotes the rate constant for activity entering the trapped compartment from the plasma compartment directly (i.e., without traversing the reversible compartment). Also, if the plasma input function approaches zero at late-time, the total activity concentration in a ROI approaches $K_i \int_0^\infty C_p(\tau) d\tau$.

3.3. Kinetic parameters as a function of ROI size

Seven sizes of ROI, 1, 4, 9, 16, 25, 50, and 100 voxels, were selected and centered on the hypoxic tumor region. Both "estimate-and-average" and "average-and-estimate" ROI *%stddev* were calculated for these 1000 noisy dynamic image samples and their corresponding kinetic parameter images. The ROI *%bias* for the late-time image and various kinetic parameters vary randomly within a small range (<2%) and are independent of the ROI size. Both the "estimate-and-average" and "average-and-estimate" give very similar result in ROI *%stddev*. Figure 7 displays the "estimate-and-average" ROI *%stddev* of various kinetic parameters (vertical axis) versus the ROI *%stddev* of the late-time image (horizontal axis) as a function of region size. The data points on each curve from right to left correspond to ROIs from small to large sizes. The ROI *%stddev*s of k_1, k_2, k_3, K_i and β decrease as the ROI size increases, but not as much as those of the late-time image. For example, increasing the size of

the ROI from 1 voxel to 100 voxels, the ROI *%stddev* of the late-time image reduces by a factor of *10* (due to the approximate Poisson nature of the simulated image noise); while the ROI *% stddev* of various kinetic parameters reduces only by a factor of *2.5~3.0*. Interestingly, the fact that both "estimate-and-average" and "average-and-estimate" give very similar ROI *% stddev*, suggests that at 15% low noise level, the pharmacokinetic model behaves like a linear operator. Thus it is acceptable to first estimate the voxelized kinetic parameter map, and then select ROI that contains similar kinetic parameter, and average the kinetic parameter over the ROI to reduce the statistical noise, i.e., using the "estimate-and-average" approach instead of the "average-and-estimate" approach.

3.4. Impact of peak-to-tail ratio in input function

The peak-to-tail ratio of the input function listed in section 3.1 is *9:1*, which corresponds to the median peak-to-tail ratio of the clinical input function. To simulate a low (*4.5:1*) and high (*18:1*) peak-to-tail ratio input function, *A0=1.38e+5* Bq/(ml·min) and *A0=8.04e+5* Bq/(ml·min) were used, respectively, where other input function parameters are the same as section 3.1. Similar dynamic images as figure 5 were simulated with the same kinetic parameter sets as shown in table 1. Figure 8 displays the noise-free TACs in the hypoxic tumor region for 3 different input functions. Despite their different height of peak at early-time, they have about the same tail height at late-time. Similar 1000 noisy samples of dynamic images were generated for both low and high peak input function at the same 15% noise level. Table 4 displays the *% stddev* of various kinetic parameters at a single voxel centered in the hypoxic tumor region from 1000 noisy samples with LS estimation for three input functions. The more peaked input function generates the more stable kinetic parameter estimation, e.g., the *%stddev* for k_3 are *20.4*, *13.5* and *9.04* respectively for low, medium and high peak input function. Figure 9 shows the (k_1, k_2) (left column) and (k_3, β) (right column) scatter plots at a single voxel in the hypoxic tumor region from 1000 noisy samples for low, medium and high peak input functions (listed as the top, middle and bottom rows). Each point in the scatter plot corresponds to a noise realization. Thus there are 1000 points in each scatter plot. Each estimated kinetic parameter is displayed as a ratio of its true kinetic parameter. Thus point *(1, 1)* (indicated as the "+" sign) in each scatter plot corresponds to the true position of each pair of kinetic parameters. Despite the correlation between each parameter pair, the scatter plot spreads out more for the low peak input function, and becomes more clustered around the true position for the high peak input function. Therefore, it is preferable to use a fast bolus injection to create a high peak input function and set a high voxel intensity threshold to capture the high peak of the image-based input function.

3.5. Impact of distortions in input function

Various distortions in the plasma input function which were considered are shown in figure 10. Except the distorted input function, the same noise-free dynamic data set as section 3.1 were used, with the same true input function parameters and true kinetic parameters. Table 5 displays the *%bias* for various distortions at a single voxel centered in the hypoxic tumor region using LS estimation. Without noise, a 30% down-shift error in its peak-amplitude causes 18.8% bias on k_3 or 24.2% bias on K_i in the hypoxic tumor region. Note that in clinical PET imaging, a 30% contrast loss is quite common for high contrast fine structures, such as the carotid artery. However, due to the limited spatial resolution, over 100% contrast recovery is rarely seen in clinical PET imaging. Thus there was no up-shift error introduced in the peak-amplitude of the input function. In peak-location, a +10sec right shift overestimates the k_3 in the hypoxic region by 25.8% or underestimates the K_i by 17.1%; while the −10sec peak left shift only overestimates k_3 by 2.8% or underestimates K_i by 2.6%. This suggests that a "late" injection (i.e., starting the PET dynamic data acquisition earlier than bolus injection that delays the peak of the plasma input function) would over-estimate a hypoxic tumor more than an "early" injection. Fortunately, this situation is easy to correct in dynamic data analysis. We only need to shift the

data to the right starting point. Therefore, capturing the correct peak-amplitude of the input function is more crucial in hypoxia imaging analysis than the peak-location.

4. Conclusion and Discussion

Compartmental analysis of dynamic PET data is considerably more time-consuming than static imaging for the patient (requiring the patient to be scanned for up to 3-hours post-injection) and for the investigator performing the data processing. However, the advantage of utilizing the kinetic information at each voxel reduces the susceptibility to statistical variations and contrast changes for a tracer whose image contrast may be close to unity. The purpose of this paper is to determine the statistical accuracy and precision of the model-based kinetic analysis, which helps to validate this analysis and provides guidance in planning clinical dynamic FMISO-PET studies.

In this paper, we have conducted the validation and sensitivity analyses of the Philips Voxulus software's implementation of an irreversible one-plasma two-tissue compartmental model for generating voxelized kinetic parametric maps of tumor hypoxia from dynamic FMISO PET studies. The analyses were performed by simulating a deterministic (i.e., with zero statistical noise) mathematical phantom with known plasma input function and various kinetic parametric tissue regions derived from actual clinical data. The noiseless kinetic parameter estimates matched their actual values exactly. We then tested its robustness for using a Gaussian-noise simulation comparable in dispersion to the actual clinical data. With *15%* noise, the FMISO-trapping rate constant k_3 (whose value is presumably related to the presence of hypoxia) varied *13.5%* in hypoxic region, at a level comparable to other kinetic parameters. Its magnitude of variation depends on the peak-to-tail ratio of the input function. A more peaked input function gave less variation in k_3. The plasma-to-diffusible tissue compartment and diffusible tissue compartment-to-plasma rate constants (k_1 and k_2, respectively) were highly correlated with each other, and both were negatively correlated with β (the ratio of tissue vasculature-to-input function); while k_3 exhibited little correlation with k_1, k_2 or β. We also observed that the influx rate constant $K_i = \frac{k_1 k_3}{k_2 + k_3}$ is potentially a more stable and direct hypoxia index than k_3.

In clinical PET imaging, photon counting noise is unavoidable. Values of kinetic parameters averaged over a multi-voxel ROI are thus preferable to single-voxel parameter values, however, important spatial information may be sacrificed. Two ROI averaging techniques were compared: "estimate-and-average" and "average-and-estimate". We found that, at *15%* low noise level, the Voxulus kinetic estimation can be approximated as a linear operator, since the statistics of the results of both approaches are equivalent to each other. Thus it is acceptable to use the more convenient "estimate-and-average" approach for easy selection of the averaging ROI. We also found that the variations of kinetic parameters reduce by increasing ROI size, but not as much as those of the late-time image, which implies that Voxulus kinetic estimation amplifies noise by a certain amount (about a factor of *3~4* at *15%* noise level).

To further investigate how bias in the arterial input function affects the kinetic parameter estimation, a shift error was introduced in the peak-amplitude and peak-location of the input TAC. We found that capturing the correct peak-amplitude and the right injecting time of the input function are crucial in hypoxia imaging analysis.

All the kinetic parameter estimation algorithms used in this paper are LS. We found that LS is more stable than WLS in Voxulus. There are two LS/WLS fittings in Voxulus: one for the plasma input function and another for tissue/tumor TAC. The fitted plasma input function is then used as input for tissue/tumor TAC fitting. In WLS, the residual error at each time point is weighted by the reciprocal of the standard deviation of each measurement. For the plasma

input function, the standard deviation of the peak measurement is higher than the tail. Thus, compared with LS, the WLS puts less weight in peak fitting than the tail fitting, which results in worse fitting at the peak of the plasma input function. For WLS estimation with data at 15% noise level, about 50 out of 1000 samples become outliners, i.e., the estimated input function does not match the measured one at all (under-fit at the peak and over-fit at the tail), and thus the estimated kinetic parameters for tumor TAC are way off from the true ones. Further, for those noisy samples with fitted input function matching the measured one, the WLS estimated C_{21} parameter in the input function can be way off from the true one (under-fit at the peak, good-fit at the tail). Any error in fitting the plasma input function will propagate into the fitting of the kinetic parameters of the tumor TAC. Thus WLS was not used in this paper.

The phantom simulated in this work assumes a perfectly stationary tumor position, which may not be the case clinically. In corresponding clinical study, data were used from radiotherapy patients with head-and-neck cancers, in which the patients were rigidly immobilized for the PET scans in a custom face mask, so tumor motion was virtually eliminated. The plasma input function in this simulation work does not consider any partial volume effect, which in a clinical study, would be derived from an artery identified in the PET/CT image, since direct arterial sampling is generally avoided. It is preferable to collect data in the thorax or abdomen region, where a large volume of arterial blood pool (such as the left ventricle or abdominal aorta) can be found and partial volume effect can be reduced. The temporal sampling in this simulation work is coarse over the first 5-minute post-injection, which thereby under-samples the sharp peak of the input function in clinics. The availability of list-mode acquisition on PET scanners will allow optimum image frame times to be selected to satisfy adequate time sampling and adequate count statistics for future studies. Future work applying the Voxulus kinetic modeling tool to patient data is needed to demonstrate the feasibility of this approach. A test-re-test study of the same patient and bootstrap re-sampling of the list-mode dynamic data to derive multiple samples of the dynamic images is needed to confirm that the standard deviations of various kinetic parameters predicted from our analysis borne out in practice.

References

Barrett HH, Wilson DW, Tsui BMW. Noise properties of the EM algorithm: I theory. Phys. Med. Biol 1994;39:833–846. [PubMed: 15552088]

Blomquist G. Maps of receptor binding parameters in the human brain – a kinetic analysis of PET measurements. Eur. J. Nucl. Med 1990;16:257–265. [PubMed: 2112470]

Brizel DM, Scully SP, Harrelson JM, Layfield LJ, Bean JM, Prosnitz LR, Dewhirst MW. Tumor oxygenation predicts for the likelihood of distant metastases in human soft tissue sarcoma. Cancer Res 1996;56:941–943. [PubMed: 8640781]

Brizel DM, Sibley GS, Prosnitz LR, Scher RL, Dewhirst MW. Tumor hypoxia adversely affects the prognosis of carcinoma of the head and neck. Int. J. Radiat. Oncol. Biol. Phys 1997;38:285–289. [PubMed: 9226314]

Brown JM, Siim BG. Hypoxia-Specific Cytotoxins in Cancer Therapy. Semin. Radiat. Oncol 1996;6:22–36. [PubMed: 10717159]

Casciari J, Graham MM, Rasey JS. A modeling approach for quantifying tumor hypoxia with [F-18] fluoromisonidazole PET time-activity Data. Med. Phys 1995;22:1127–1139. [PubMed: 7565388]

Chapman JD, Lee J, Meeker BE. Keynote address: cellular reduction of nitroimidazole drugs: potential for selective chemotherapy and diagnosis of hypoxic cells. Int. J. Radiat. Oncol. Biol. Phys 1989;16:911–917. [PubMed: 2649465]

Dehdashti F, Grigsby PW, Mintun MA, Lewis JS, Siegel BA, Welch MJ. Assessing tumor hypoxia in cervical cancer by positron emission tomography with 60Cu-ATSM: relationship to therapeutic response-a preliminary report. Int. J. Radiat. Oncol. Biol. Phys 2003;55:1233–1238. [PubMed: 12654432]

Evans SM, et al. Noninvasive detection of tumor hypoxia using the 2-nitroimidazole [18F]EF1. J. Nucl. Med 2000;41:327–336. [PubMed: 10688119]

Fyles AW, et al. Oxygenation predicts radiation response and survival in patients with cervix cancer. Radiother. Oncol 1998;48:149–156. [PubMed: 9783886]

Höckel M, Knoop C, Schlenger K, Vorndran B, Bauβmann E, Mitze M, Knapstein PG, Vaupel P. Intratumoral pO2 predicts survival in advanced cancer of the uterine cervix. Radiother. Oncol 1993;26(1):45–50. [PubMed: 8438086]

Huang, S-C.; Phelps, ME. Principle of Tracer Kinetic Modeling in Positron Emission Tomography and Autoradiography. New York: Raven Press; 1986. Chapter 7; p. 287-345.

Knocke TH, Weitmann HD, Feldmann HJ, Selzer E, Pötter R. Intratumoral pO2-measurements as predictive assay in the treatment of carcinoma of the uterine cervix. Radiother. Oncol 1999;53:99–104. [PubMed: 10665785]

Lee NY, et al. Fluorine-18-labeled fluoromisonidazole positron emission and computed tomography-guided intensity-modulated radiotherapy for head and neck cancer: a feasibility study. Int. J. Radiat. Oncol. Biol. Phys 2008;70:2–13. [PubMed: 17869020]

Lehtiö K, Oikonen V, Nyman S, Grönroos T, Roivainen A, Eskola O, Minn H. Quantifying tumour hypoxia with fluorine-18 fluoroerythronitroimidazole ([18F]FETNIM) and PET using the tumour to plasma ratio. Eur. J. Nucl. Med. Mol. Imaging 2003;30:101–108. [PubMed: 12483416]

Lehtiö K, Eskola O, Viljanen T, Oikonen V, Grönroos T, Sillanmäki L, Grénman R, Minn H. Imaging perfusion and hypoxia with PET to predict radiotherapy response in head-and-neck cancer. Int. J. Radiat. Oncol. Biol. Phys 2004;59:971–982. Erratum in: *Int. J. Radiat. Oncol. Biol. Phys.***60** 1010. [PubMed: 15234030]

Lewis JS, Sharp TL, Laforest R, Fujibayashi Y, Welch MJ. Tumor uptake of copper-diacetyl-bis(N(4)-methylthiosemicarbazone): effect of changes in tissue oxygenation. J. Nucl. Med 2001;42:655–661. [PubMed: 11337556]

Movsas B, Chapman JD, Horwitz EM, Pinover WH, Greenberg RE, Hanlon AL, Lyer R, Hanks GE. Hypoxic regions exist in human prostate carcinoma. Urology 1999;53:11–18. [PubMed: 9886581]

Nehmeh SA, et al. Reproducibility of intratumor distribution of (18)F-fluoromisonidazole in head and neck cancer. Int. J. Radiat. Oncol. Biol. Phys 2008;70:235–242. [PubMed: 18086391]

Nordsmark M, Overgaard M, Overgaard J. Pretreatment oxygenation predicts radiation response in advanced squamous cell carcinoma of the head and neck. Radiother. Oncol 1996;41:31–39. [PubMed: 8961365]

Rajendran JG, et al. [(18)F]FMISO and [(18)F]FDG PET imaging in soft tissue sarcomas: correlation of hypoxia, metabolism and VEGF expression. Eur. J. Nucl. Med .Mol. Imag 2003;30:695–704.

Rajendran JG, Mankoff DA, O'Sullivan F, Peterson LM, Schwartz DL, Conrad EU, Spence AM, Muzi M, Farwell DG, Krohn KA. Hypoxia and glucose metabolism in malignant tumors: evaluation by [18F]fluoromisonidazole and [18F]fluorodeoxyglucose positron emission tomography imaging. Clin. Cancer. Res 2004;10:2245–2252. [PubMed: 15073099]

Rajendran JG, Schwartz DL, O'Sullivan J, Peterson LM, Ng P, Scharnhorst J, Grierson JR, Krohn KA. Tumor hypoxia imaging with [F-18] fluoromisonidazole positron emission tomography in head and neck cancer. Clin. Cancer. Res 2006;12:5435–5441. [PubMed: 17000677]

Rasey JS, Koh WJ, Evans ML, Peterson LM, Lewellen TK, Graham MM, Krohn KA. Quantifying regional hypoxia in human tumors with positron emission tomography of [18F]fluoromisonidazole: a pretherapy study of 37 patients. Int. J. Radiat. Oncol. Biol. Phys 1996;36:417–428. [PubMed: 8892467]

Riedl CC, et al. Imaging hypoxia in orthotopic rat liver tumors with iodine 124-labeled iodoazomycin galactopyranoside PET. Radiology 2008;248:561–570. [PubMed: 18641253]

Sorger D, Patt M, Kumar P, Wiebe LI, Barthel H, Seese A, Dannenberg C, Tannapfel A, Kluge R, Sabri O. 18F Fluoroazomycin arabinofuranoside (18FAZA) and 18F fluoromisonidazole (18FMISO): A comparative study of their selective uptake in hypoxic cells and PET imaging in experimental rat tumors. Nucl. Med. Biol 2003;30:317–326. [PubMed: 12745023]

Tatum JL, et al. Hypoxia: importance in tumor biology, noninvasive measurement by imaging, and value of its measurement in the management of cancer therapy. Int. J. Radiat. Biol 2006;82(10):699–757. [PubMed: 17118889]

Thomlinson RH, Gray LH. The histological structure of some human lung cancers and the possible implications for radiotherapy. Br. J. Cancer 1955;9:539–549. [PubMed: 13304213]

Thorwarth D, Eschmann SM, Paulsen F, Alber M. A Kinetic model for dynamic [18F]-Fmiso PET data to analyze tumor hypoxia. Phy. Med. Biol 2005a;50:2209–2224.

Thorwarth D, Eschmann SM, Scheiderbauer J, Paulsen F, Alber M. Kinetic analysis of dynamic 18F-fluoromisonidazole PET correlates with radiation treatment outcome in head-and-neck cancer. BMC Cancer 2005b;5:152. [PubMed: 16321146]

Vergis R, et al. Intrinsic markers of tumour hypoxia and angiogenesis in localised prostate cancer and outcome of radical treatment: a retrospective analysis of two randomised radiotherapy trials and one surgical cohort study. Lancet. Oncol 2008;9:342–351. [PubMed: 18343725]

Wilson DW, Tsui BMW, Barrett HH. Noise properties of the EM algorithm: II Monte Carlo simulations. Phys. Med. Biol 1994;39:847–871. [PubMed: 15552089]

Yang DJ, Wallace S, Cherif A, Li C, Gretzer MB, Kim EE, Podoloff DA. Development of F-18-labeled fluoroerythronitroimidazole as a PET agent for imaging tumor hypoxia. Radiology 1995;194:795–800. [PubMed: 7862981]

Zanzonico P, et al. Iodine-124-labeled iodo-azomycin-galactoside imaging of tumor hypoxia in mice with serial microPET scanning. Eur. J. Nucl. Med. Mol. Imag 2004;31:117–128.

Ziemer LS, Evans SM, Kachur AV, Shuman AL, Cardi CA, Jenkins WT, Karp JS, Alavi A, Dolbier WR Jr, Koch CJ. Noninvasive imaging of tumor hypoxia in rats using the 2-nitroimidazole 18F-EF5. Eur. J. Nucl. Med. Mol. Imag 2003;30:259–266.

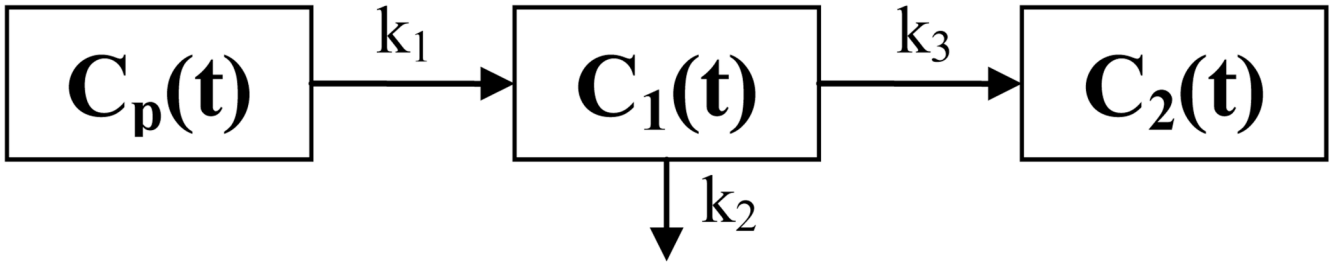

Figure 1.
Generic irreversible one-plasma two-tissue compartmental model.

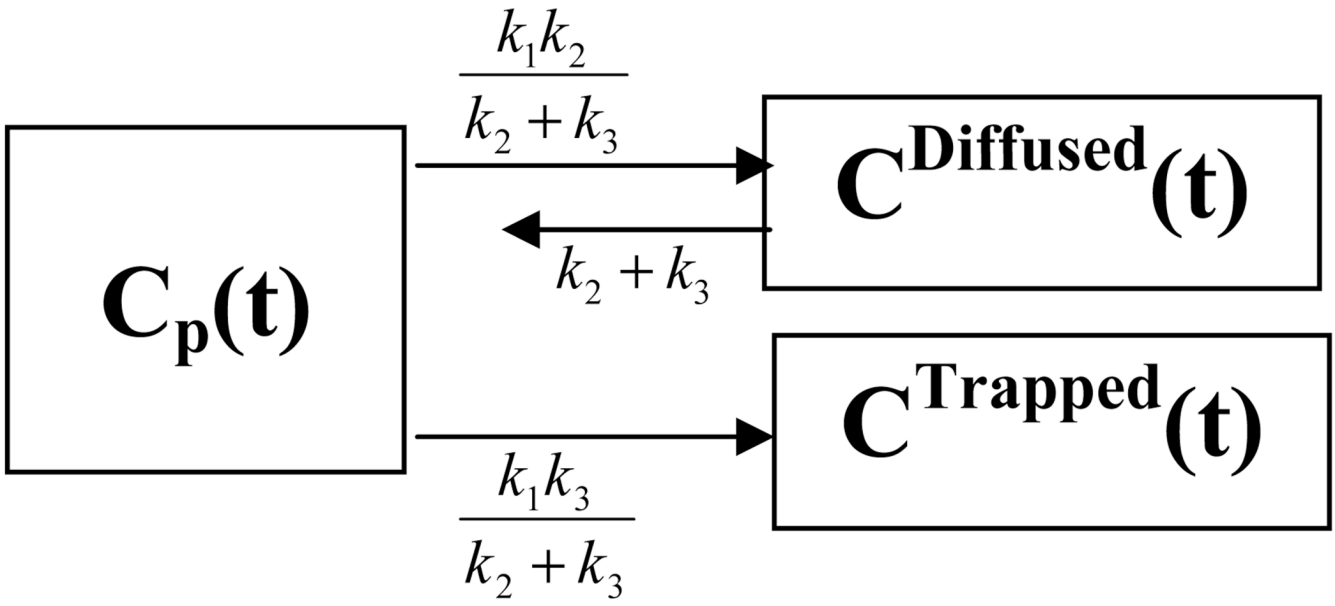

Figure 2.
Two decoupled single-tissue compartmental models.

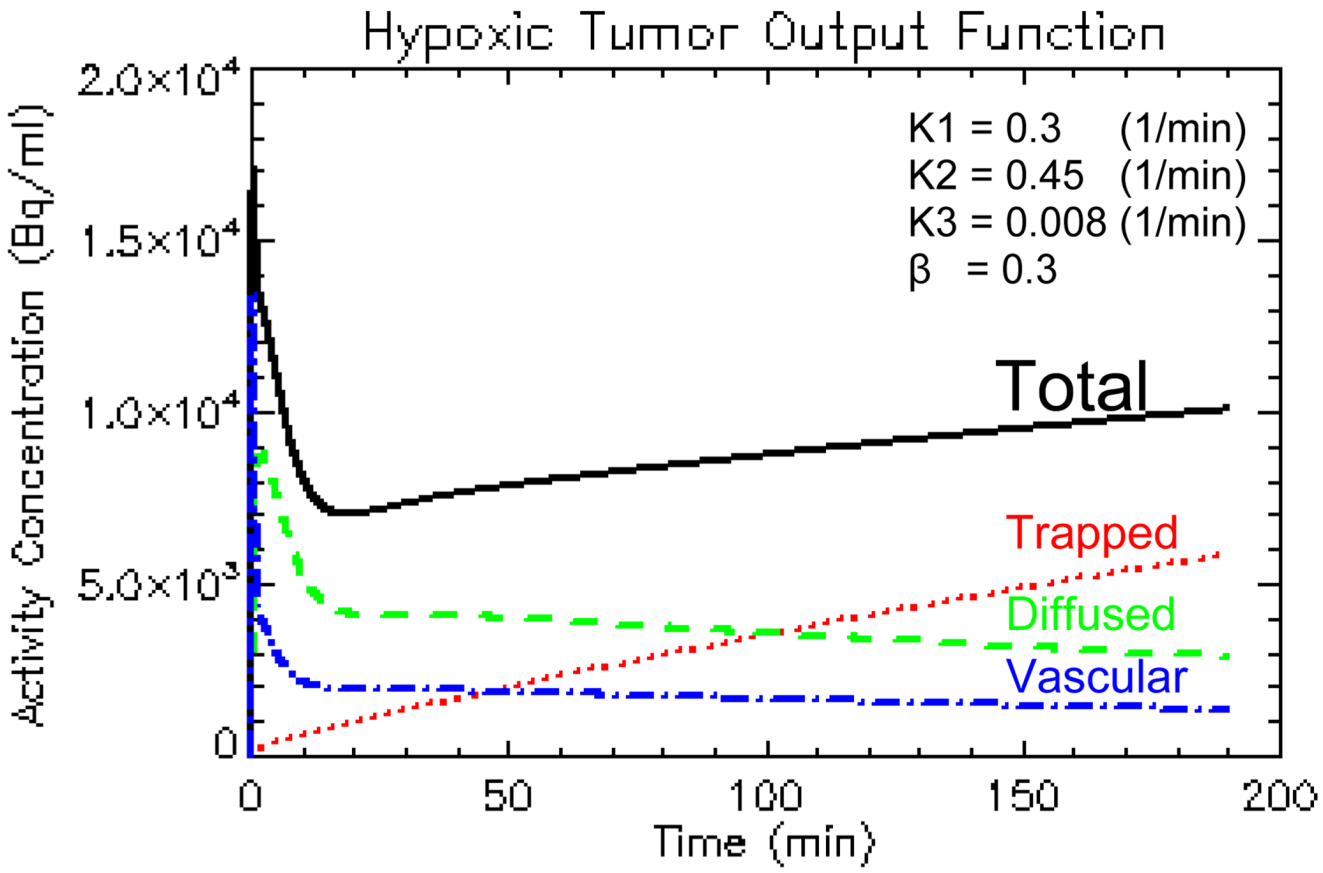

Figure 3.
The total time-activity-curve as a decomposition of vascular, diffused and trapped components.

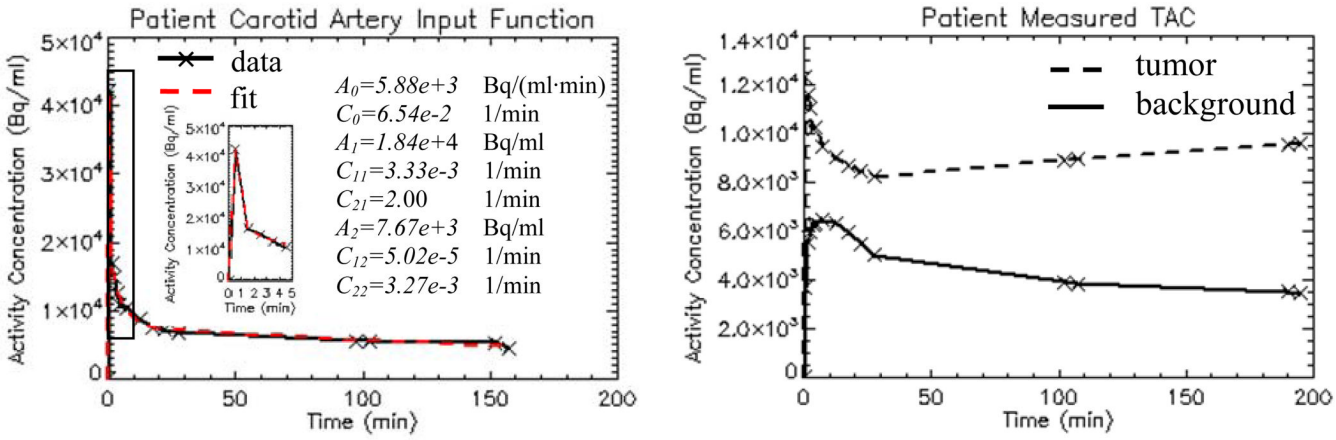

Figure 4.
Head-and-neck cancer patient's TAC of input function from carotid artery (a), and TACs of tumor and background soft tissue regions (b).

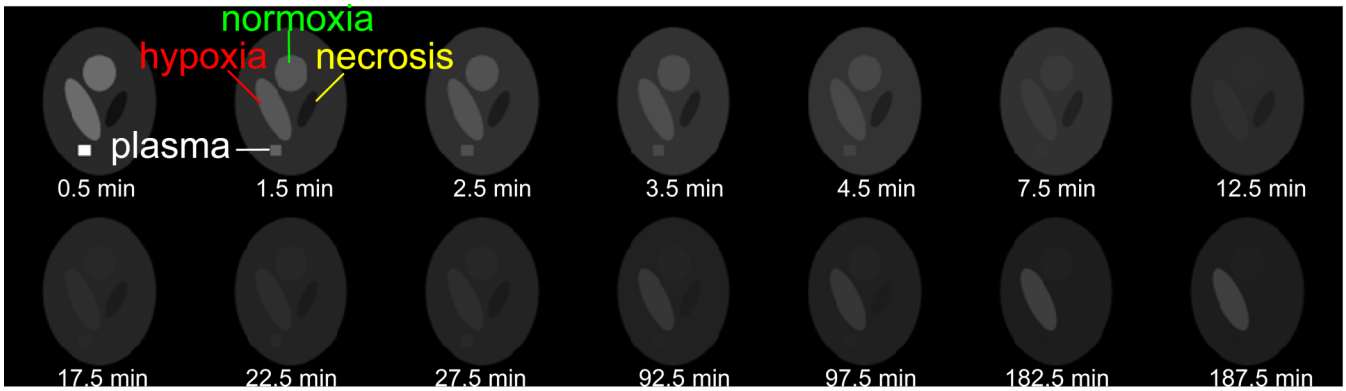

Figure 5.
Simulated noise-free images of multiple dynamic frames.

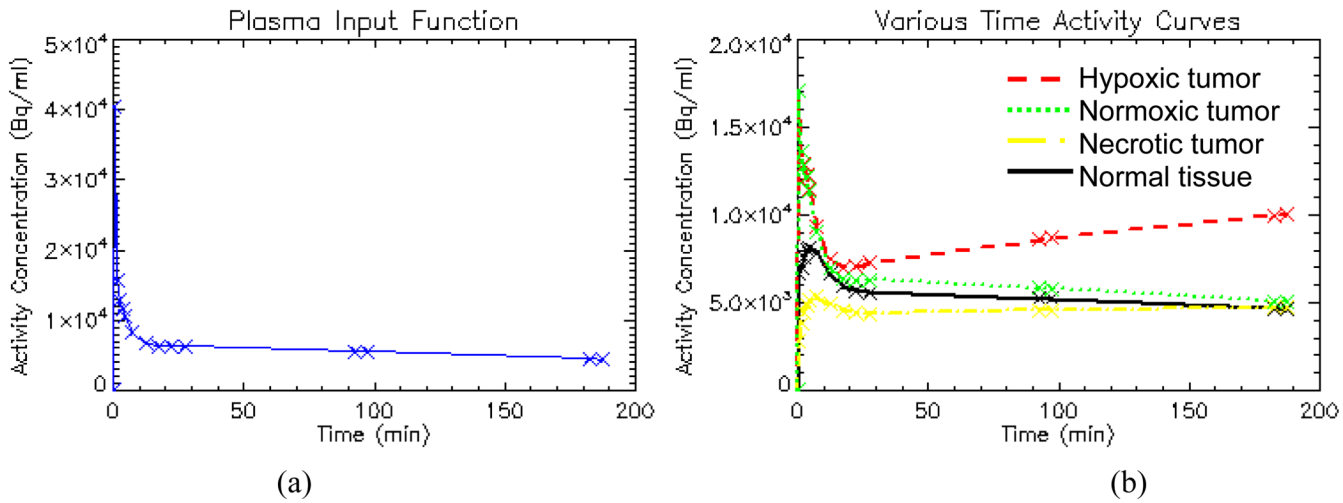

Figure 6.
Simulated noise-free plasma input function (a) and noise-free time-activity-curves for various tissue regions (b).

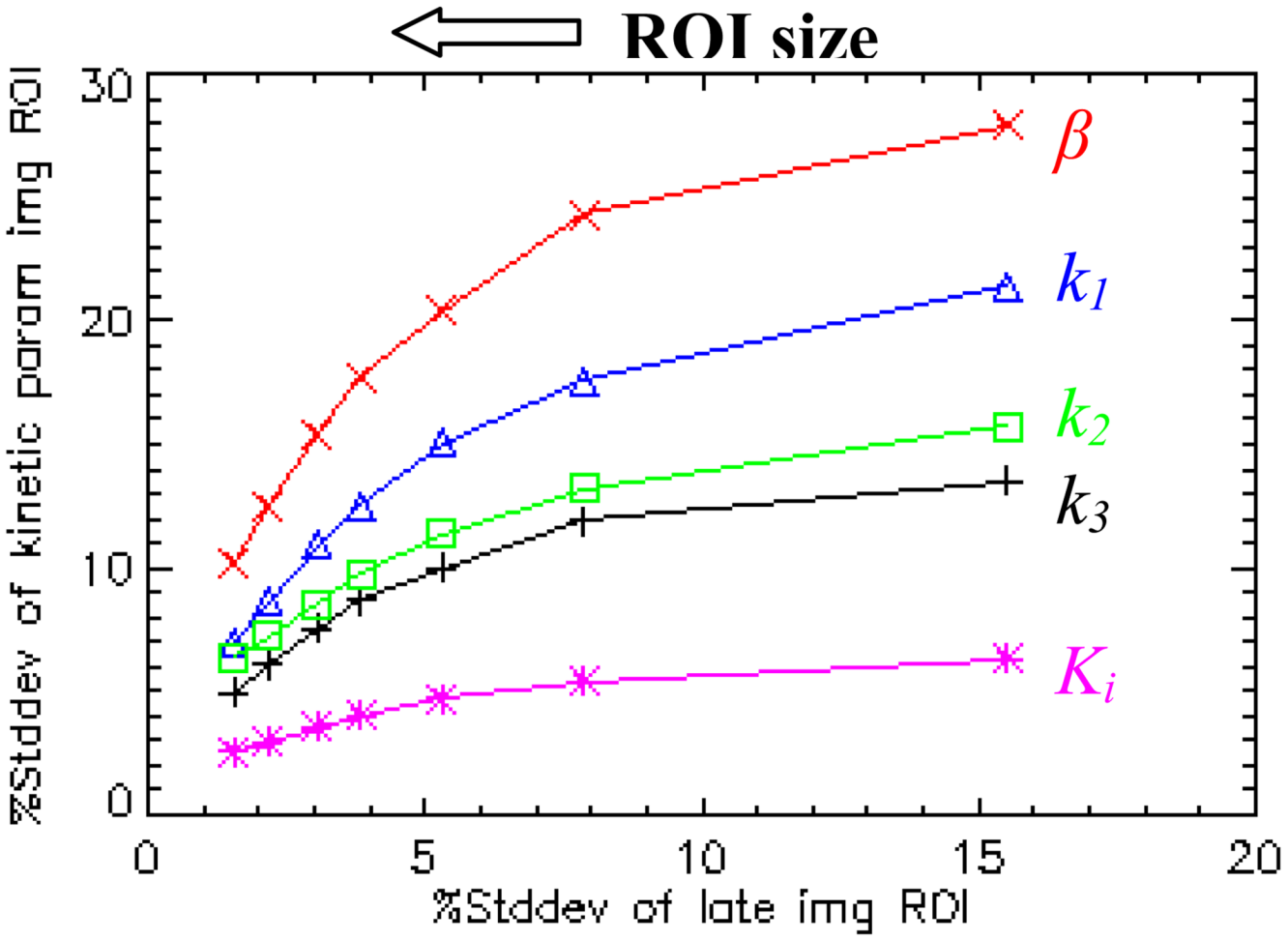

Figure 7.

ROI *%stddev* of late-time image and various kinetic parameter images in hypoxic region as a function of ROI size for 1000 noisy samples with LS estimation. The curves from top to bottom are β (x), k_1 (Δ), k_2 (□), *k3* (+) and *Ki* (*), respectively.

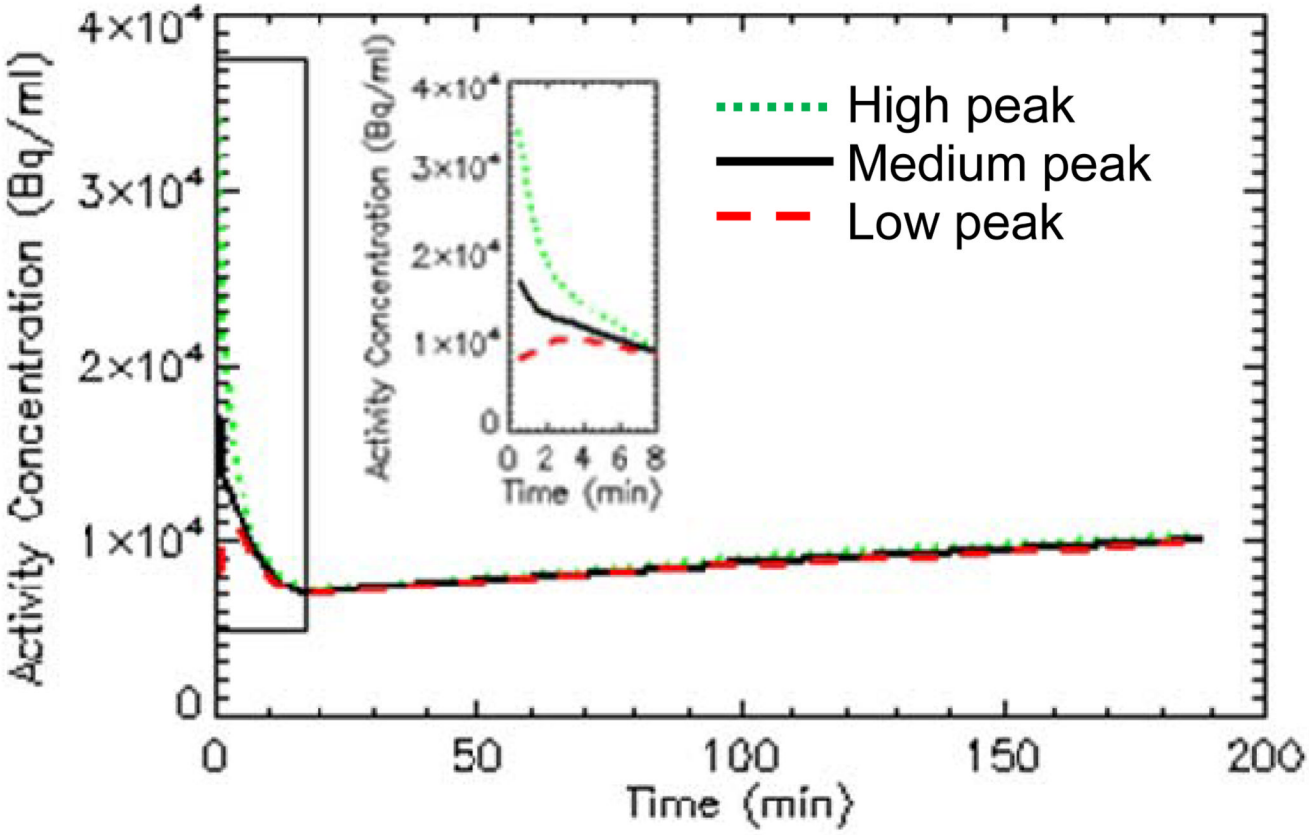

Figure 8.
Hypoxic tumor noise-free time-activity-curves for low (dashed line), medium (solid line), and high (dotted line) peak-to-tail ratio input functions.

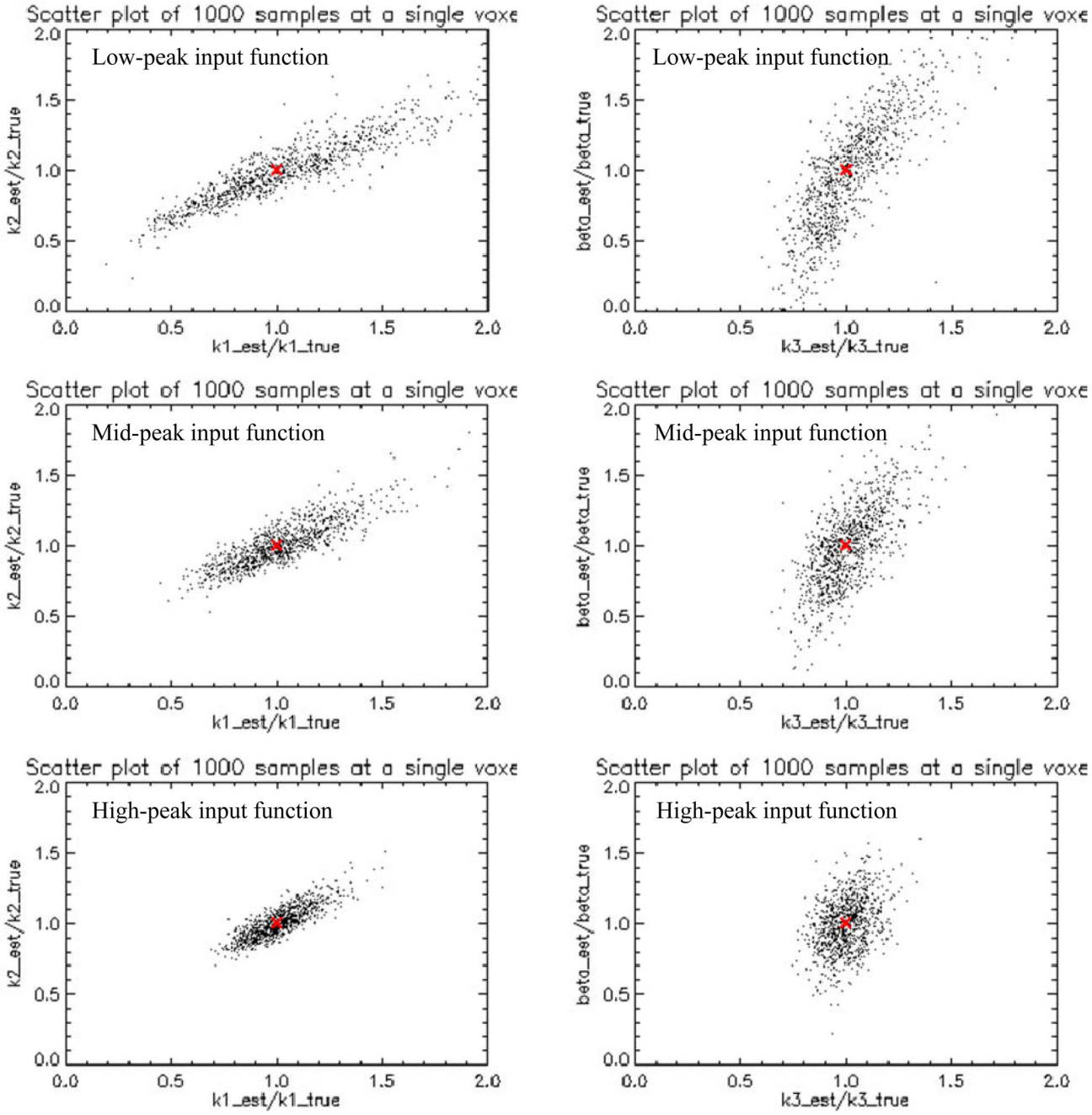

Figure 9.

Scatter plots of various estimated kinetic parameters centered at a single voxel in the hypoxic tumor region from 1000 noisy samples for different peak-height input function. Left column: k_1 versus k_2, right column: k_3 versus β. Top row: low-peak input function, middle row: medium-peak input function, bottom row: high-peak input function.

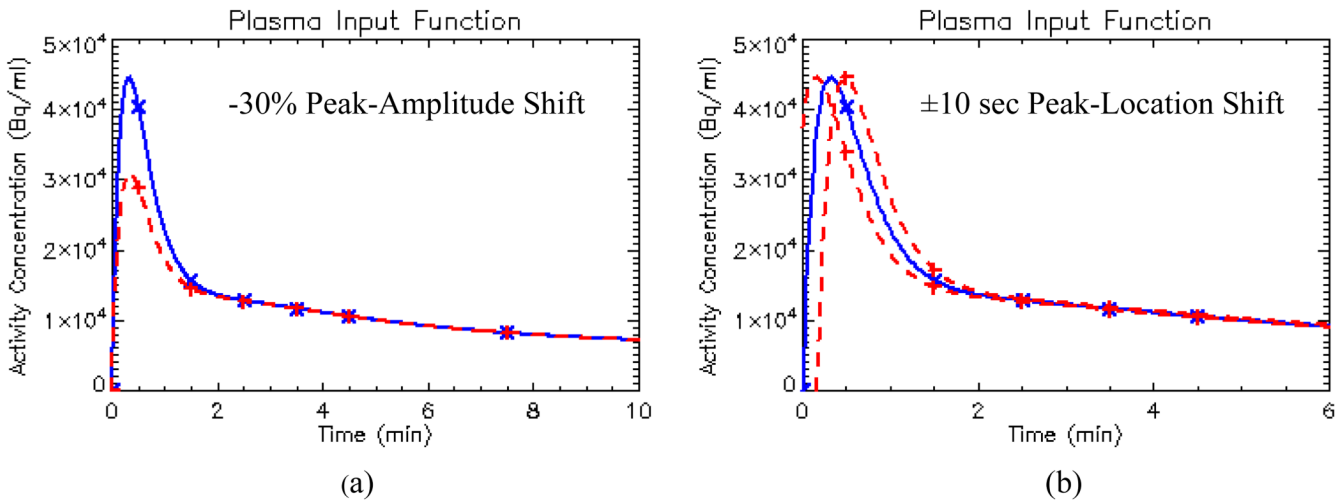

Figure 10.
Illustration of various distortions in input function: (a) −30% peak amplitude shift; (b) ±10 sec peak location shift. The original input function is shown in solid line with “x’ sign, the shifted ones are shown with dashed line with “+” sign.

Table 1

True kinetic parameters for simulated image dataset.

	Hypoxic Tumor	Necrotic Tumor	Normoxic Tumor	Normal Tissue
k_1 (1/min)	0.30	0.09	0.30	0.15
k_2 (1/min)	0.45	0.15	0.45	0.20
k_3 (1/min)	8e-3	3e-3	1e-3	1e-3
β	0.3	0.03	0.3	0.1
K_i (1/min)	5.24e-3	1.76e-3	6.65e-4	7.46e-4

Table 2

% *bias* and % *stddev* at a single voxel in various tissue regions for 1000 noisy samples with LS estimation.

LS		% Bias	% Stddev
Hypoxic Tumor	k_1 (1/min)	1.97	21.4
	k_2 (1/min)	1.01	15.7
	k_3 (1/min)	0.97	13.5
	β	−1.13	27.9
	K_i (1/min)	0.19	6.30
Necrotic Tumor	k_1 (1/min)	−2.92	11.5
	k_2 (1/min)	−2.05	10.7
	k_3 (1/min)	0.66	15.9
	β	28.2	81.8
	K_i (1/min)	−0.80	13.3
Normoxic Tumor	k_1 (1/min)	1.74	20.1
	k_2 (1/min)	1.10	14.9
	k_3 (1/min)	0.56	42.9
	β	−1.04	28.2
	K_i (1/min)	−0.45	40.6
Normal Tissue	k_1 (1/min)	−1.32	13.0
	k_2 (1/min)	*−0.91*	10.3
	k_3 (1/min)	*0.79*	35.0
	β	*4.97*	43.9
	Ki (1/min)	*−0.65*	32.6

Table 3

Correlation coefficient at a single voxel in various tissue regions for 1000 noisy samples with LS estimation.

LS	$\rho(k_1, k_2)$	$\rho(k_1, k_3)$	$\rho(k_2, k_3)$	$\rho(k_1, \beta)$	$\rho(k_2, \beta)$	$\rho(k_3, \beta)$	$\rho(K_i, \beta)$
Hypoxic Tumor	0.85	−0.47	−0.01	−0.80	−0.43	0.69	−0.27
Necrotic Tumor	0.92	0.02	0.28	−0.77	−0.56	0.09	−0.14
Normoxic Tumor	0.81	0.14	0.41	−0.78	−0.32	0.01	−0.26
Normal Tissue	0.91	0.04	0.27	−0.80	−0.54	0.03	−0.13

Table 4

%*stddev* at a single voxel centered in the hypoxic tumor region for low, medium, and high peak input function from 1000 noisy samples with LS estimation.

%*stddev*	**Low Peak-to-Tail (4.5:1)**	**Med Peak-to-Tail (9:1)**	**High Peak-to-Tail (18:1)**
k_1 (1/min)	36.6	21.4	12.6
k_2 (1/min)	32.5	15.7	10.9
k_3 (1/min)	20.4	13.5	9.04
β	40.9	27.9	18.5
Ki (1/min)	9.91	6.30	6.00

Table 5

%*bias* at a single voxel centered in the hypoxic tumor region for −30% peak-amplitude shift and ±10sec peak-location shift in input function for LS estimation without any noise.

%*Bias*	−30% Peak Amplitude Shift	+10sec Peak Location Shift	−10sec Peak Location Shift
k_1 (1/min)	15.7	−91.3	16.1
k_2 (1/min)	42.4	−88.8	22.9
k_3 (1/min)	18.8	25.8	2.8
β	53.0	105.3	21.4
Ki (1/min)	24.2	−17.1	−2.6